A Gravity Compensation System for Touchdown Process Verification of Large Spacecraft With Quasi-Zero Stiffness Mechanism and Passivity-Based Controller

Rongqiao Zhang, Zhengqing Li, Haining Sun, *Member, IEEE*, and Xiaoqaing Tang

***Abstract*—To ensure the reliability of an extraterrestrial lander during its touchdown process, it is crucial to replicate the landing dynamics within a simulated low-gravity environment. In this study, a servo-driven system(SDS) is proposed and integrated with a quasi-zero stiffness(QZS) system to address the limitations of traditional methods, including restricted accuracy and limited movement range. An analytical method for describing the dynamic characteristics of the low-gravity simulation system is presented based on passivity theory, enhancing the compensation accuracy. Subsequently, a fuzzy controller for the QZS-SDS composite system is designed to autonomously adjust the equilibrium point and convergence speed, ensuring rapid error reduction in tension control. Furthermore, the global asymptotic stability conditions of the closed-loop system are established and analyzed, and the quantitative parameter design guidelines for practical implementation are provided. Finally, a series of physical experiments demonstrate the efficiency and robustness of the proposed system. Compared to conventional methods using only QZS, the proposed approach reduces the maximum force compensation error from 13.9% to 4.0%, and extends the supported simulation range from 800mm to over 12,000mm.**

***Note to Practitioners*—This study addresses the challenges of providing a reliable low-gravity environment for the touchdown phase of extraterrestrial landers. The primary motivation is to verify the robustness of the engine shutdown algorithm and evaluate the strength/stiffness design of the landing legs under realistic impact conditions. While some low-gravity compensation systems have been widely used in orbiting and descent phases, their effectiveness during the touchdown process, where strong impacts occur, remains insufficiently explored. At higher landing velocities(approximately 1.1 m/s), most low-gravity compensation systems struggle to maintain accuracy due to bandwidth limitations, except for quasi-zero stiffness(QZS) systems. However, QZS-based approaches suffer from mechanical deviations such as stiffness inconsistencies in energy storage components and friction, leading to reduced compensation accuracy. Additionally, the movement range of QZS is constrained by mechanical structures, restricting their application in spacecraft landing missions. To overcome these limitations, we propose an actively controlled servo-drive system with a passivity-based control law for precise force compensation. The introduction of servo motors not only improves compensation accuray but also significantly extends the system's operational range, enabling it to meet the requirements of various landing tasks. This work has direct implications for practitioners developing ground-based low-gravity simulation systems for extraterrestrial exploration. In the future, we aim to extend our low-gravity compensation technology to support extraterrestrial launch missions, broadening its application from single-degree-of-freedom landing tasks to multi-degree-of-freedom non-vertical take-off scenarios.**

***Index Terms*—Gravity compensation system, ground verification, passivity-based control, quasi-zero stiffness, underactuated mechanical systems.**

Received 20 March 2025; revised 2 July 2025; accepted 16 August 2025. Date of publication 20 August 2025; date of current version 5 September 2025. This article was recommended for publication by Associate Editor X. Li and Editor S. Takai upon evaluation of the reviewers' comments. This work was supported by the National Natural Science Foundation of China under Grant 52575024. *(Rongqiao Zhang and Zhengqing Li contributed equally to this work.) (Corresponding authors: Haining Sun; Xiaoqaing Tang.)*

Rongqiao Zhang, Zhengqing Li, and Xiaoqaing Tang are with the State Key Laboratory of Tribology in Advanced Equipment, Department of Mechanical Engineering, Tsinghua University, Beijing 100084, China (e-mail: zrq21@mails.tsinghua.edu.cn; lizhengq22@mails.tsinghua.edu.cn; tang-xq@mail.tsinghua.edu.cn).

Haining Sun is with Singapore Institute of Manufacturing Technology, Agency for Science, Technology and Research (A*STAR), Singapore 138634 (e-mail: sunhn@simtech.a-star.edu.sg).

This article has supplementary downloadable material available at https://doi.org/10.1109/TASE.2025.3600626, provided by the authors.

Digital Object Identifier 10.1109/TASE.2025.3600626

Nomenclature

Notations

$\dot{\square}$	$\partial\square/\partial t$.
$\square'$	$\partial\square/\partial x$.
$\delta\square$	Variation of $\square$.

Variables

l	Distance of QZS fulcrums vertically.
l_1	Distance of QZS lever fulcrum and spring connection posint.
l_2	Length of QZS lever.
θ	Rotation angle of QZS lever.
s	Length of QZS spring.
s_0	Original length of QZS spring.
k	Stiffness of QZS spring.
m	Mass of QZS lever.
T_f	Rotational friction of QZS lever.
T_μ	Static rotational friction of QZS lever.
C_μ	Coulomb rotational friction of QZS lever.
f	Output force of QZS on the end of rod.
x_u	Cable length released by SDS motor.
$k^\star$	Desired spring QZS stiffness.

$f^\star$	Desired output force of QZS.
δk	Stiffness deviation of QZS springs.
f_e	Output force error of QZS.
f_{dk}	Force error caused by QZS spring stiffness deviation.
$w(x,t)$	Deformation field of cable.
$u(t)$	Displacement constraint of cable on $x = 0$.
E	Young's modulus of cable.
A	Cross-section area of cable.
ρ	Linear density of cable.
L	Undeformed length of cable.
$\phi_i, i = 1, \ldots, N$	Trial functions of cable deformation field.
$q_i, i = 1, \ldots, N$	Coefficients of cable trial functions.
N	Number of cable trial functions.
M_g	Mass of the payload on the cable.
k_g	Contact stiffness of the payload with ground.
c_g	Contact damping of the payload with ground.

I. Introduction

THE moon, as Earth's sole natural satellite, has become the hotspot of human space exploration activities with the new developments in extraterrestrial exploration technologies and the discovery of new lunar resources. However, among all lunar landing missions, only 3 agencies have successfully soft-landed on the lunar surface [1]. An important factor affecting the success of lunar soft landing [2] is the reliability of the lander during the touchdown process in a low-gravity environment: In 2023, Russia's Luna 25 explorer experienced a rollover during touchdown due to the engine's failure to shut down properly [3], [4]; In 2024, the American Odysseus lunar lander suffered damage to its landing legs due to an excessively high touchdown velocity [5]. To ensure the stability and reliability of the lander during the touchdown process, it is necessary to conduct verification tests on touchdown stability in low-gravity environments on Earth [6].

Various effective methods can be employed to provide low-gravity environments, which can be categorized into 2 classes based on the simulation principles [7], [8]. One class of methods involves generating a constant force field to replicate a low-gravity environment, with typical methods including the underwater method [9], parabolic flight, and the drop tower method [7]. Some scholars also use magnetic levitation technology to provide low-gravity environments, but the experiments are still in the early stages [10]. Additionally, the air-floating method can be used to simulate a zero-gravity environment on a flat surface. However, this method restricts movement perpendicular to the plane [11], [12], [13], [14], [15]. The field force methods are generally used for small-scale tasks with light mass, such as researching material and fluid properties in a low-gravity environment [10]. These methods are unsuitable for the touchdown process verification of large-scale landers due to their limited motion range and low simulation speed.

Another approach simulates a low-gravity environment by applying a constant concentrated force at the center of mass of the experiment object, which generally uses cable-suspended counterweights [16], [17], [18], [19], series elastic actuators(SEA) [20], [21], or quasi-zero stiffness(QZS) mechanisms [22], [23] for constant force output. Unlike the orbiting or descending phases which are the majority of low-gravity researches, the touchdown process is characterized by high velocities and strong impacts. This necessitates that the simulation equipment providing the low-gravity field be capable of withstanding significant external disturbances. Furthermore, the touchdown process involves the interaction between the lander and ground, which is complicated by the ground's unstructured nature. This introduces unknown parameters, reducing compensation accuracy. Consequently, methods relying on counterweights or servo motors for constant force output face challenges due to limited response bandwidth [18].

To mitigate the impact of external disturbances on the force output of low-gravity simulation equipment, researchers have explored reducing stiffness at the force output side to enhances the system's ability against external perturbations, leading to the application of SEA in low-gravity simulation tasks [24], [25], [26], [27]. Qu directly used springs as the stiffness buffering device and employed the torque loop of a servo motor as the actuator for low-gravity compensation experiments, achieving a tension compensation error of 5%. However, the relatively high stiffness of conventional springs limited further improvement in constant force control accuracy [27]. Jia et al. designed a buffer-assisted pinion-rack mechanism to simulate the zero-gravity environment of space orbital missions and conducted experiments using a six-degree-of-freedom manipulator, achieving 95% gravity compensation accuracy [24]. Building on Jia's work, Duan et al. developed a control law based on sliding mode control and error observers, ensuring system stability under bounded external disturbances and improved force compensation accuracy [25]. It is worth noting that the SEA methods used for low-gravity compensation of spacecraft can also be applied to human rehabilitation training. By leveraging the high-precision force output and low-stiffness characteristics of SEA, precise control and support of human motion can be achieved, thereby improving the effectiveness of rehabilitation training [28].

However, the SEA mechanism's stiffness is generally non-zero, which can lead to significant force output errors when the system is subjected to strong disturbances. When the stiffness at the force output side is reduced to zero, the system's output force remains constant regardless of external disturbances, transitioning the SEA mechanism into a quasi-zero stiffness(QZS) mechanism [29], [30], [31], [32], [33], [34], [35]. There are various designs for QZS mechanisms, but generally they must ensure that the system's potential energy remains constant with respect to the output displacement. Some approaches achieve this by directly constraining the system's potential energy through special mechanism designs [36], while others realize zero-stiffness characteristics by combining structures with different stiffness properties (i.e., potential energy-displacement curves exhibiting both convex and concave segments) [35], [37]. In our previous work, a QZS based on constant force springs was designed to provide a low-gravity simulation environment, which has been successfully applied in the landing simulation test of

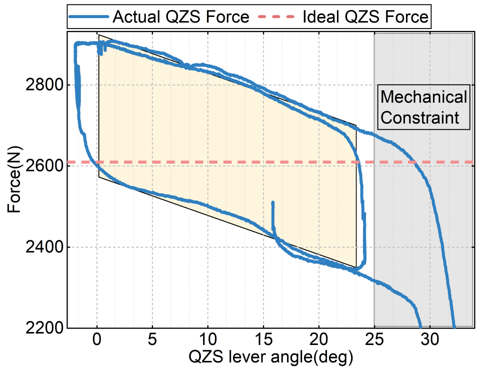

Fig. 1. The relationship between the actual force output of the QZS and the lever angle is depicted. The blue solid line reveals the relationship between the QZS output force and angle. The yellow area indicates the actual working range, while the gray shaded area represents the upper limit of the angle due to mechanical constraints. Although the theoretical QZS stiffness should be 0 N/deg, the actual measured stiffness is 8.3 N/deg due to QZS parameter deviations.

China's Mars lander, achieving a maximum compensation force error of 13.9% under 1100mm/s touchdown velocity [36]. Ding et al. proposed a novel QZS by paralleling a diamond-shaped mechanism with a nonlinear bi-stable beam, and applied it to a vibration isolation platform, achieving a resonance frequency of 0.18 Hz [38]. Liu and Niu directly embedded the compression springs and torsion bar into the output winch, realizing a pulley-free QZS mechanism and increasing the output bandwidth to 6 Hz. Under an excitation input of 17 mm/s, the tension regulation accuracy reached 96% [34], [35]. Zhou et al. introduced a QZS mechanism based on magnetic negative stiffness springs to provide a low-gravity environment for the spacecraft under 200mm movement range. Due to the frictionless feature of the magnetic QZS supporting unit, the system achieved a maximum compensation force error of 0.7% under 400mm/s collision test [31].

However, subsequent testing identified certain deficiencies in using QZS alone for low-gravity simulation. One key issue is the accuracy of compensation force, which is entirely dependent on the mechanism's integrity. Any deviations in the mechanism's parameters can lead to increased errors in force output. For example, since the force generated by QZS is directly related to the stiffness of the energy-storing elements(such as springs), inevitable discrepancies between the designed and actual stiffness values lead to reduced precision in the output force. Additionally, the significant output force of low-gravity simulation devices causes non-negligible frictional effects in the QZS, further compromising the precision of the force output. A set of QZS output force and movement angle curves is depicted in Fig. 1. Ideally, the output force should be independent of the lever angle, but due to the presence of friction and spring stiffness errors, the force output curve shows deviations. Another challenge is the limited movement range provided by QZS. To meet the varying stroke and velocity requirements of different simulation objectives, it is necessary to expand the motion range of the low-gravity simulation device, that is difficult to achieve with QZS alone.

To address the aforementioned issues, this study introduces an additional motor in conjunction with QZS for active force control. By using a force sensor to feedback the actual force applied to the lander, the motor can compensate for force errors caused by QZS deviations. Additionally, the incorporation of the motor significantly expands the system's operation range. There is currently little research that combines quasi-zero stiffness (QZS) systems with motor-driven active tension control under strong disturbances, as achieving stable and precise regulation in such conditions remains highly challenging. Since the cable-driven mechanism is an under-actuated system with infinite degrees-of-freedoms, it is difficult to estimate the internal states by measuring the output force alone. Therefore, the designed controller should stabilize the system through output feedback [39]. Furthermore, the force sensor and the motor are non-collocated in general cable-driven mechanisms [40], which complicates controller design. Finally, designing and analyzing controllers for the coupled nonlinear system with cable-driven mechanism and the QZS subsystem poses a significant challenge.

To design an appropriate output feedback controller, we first analyzed the dynamic input-output characteristics of the QZS and the cable-lander subsystem using passivity theory [41], [42], [43], demonstrating that relying solely on the QZS for force compensation leads to accuracy issues when there are stiffness deviations and friction in the QZS. Subsequently, to ensure the stability of the composite system, we utilized the stability theorem for interconnected systems to analyze the conditions that the active controller should met. Finally, a fuzzy controller was designed to guarantee the globally asymptotic stability of the closed-loop system. Simulations and experiments demonstrated the effectiveness of the designed controller and the low-gravity compensation system.

The contributions of this paper are summarized as follows:

1) An analysis method based on passivity theory is proposed for describing the dynamic characteristics of a gravity compensation system(GCS), which reveals the limitations of using only QZS for low gravity simulation. The results indicate that in the presence of deviations in mechanism parameters, the force compensation error of QZS alone can reach up to 7.1%, which can be reduced to 1.9% with the active force control.
2) A fuzzy controller is designed for the hybrid system combining QZS mechanisms and motors, which can autonomously adjust the system's equilibrium point and convergence speed, ensuring rapid convergence of tension control errors. The conditions for global asymptotic stability of the closed-loop system are established, and the controller's robustness against external disturbances is demonstrated under different circumstances(such as touchdown stiffness and velocity). Moreover, quantitative guidelines for the design parameters of the GCS in practical applications are provided.
3) Touchdown experiments are conducted on a self-built physical platform, and the results confirmed the effectiveness and robustness of the proposed method. At a touchdown speed of 1.1 m/s, the maximum tension control error is only 4%. A comparison with other low gravity simulation methods is provided in Table I, demonstrating that the system proposed in this study

TABLE I

GCS Compensation Results of Multiple Methods

Method	Velocity (mm/s)	Movement Range (mm)[1]	Payload (kg)	Force Error
Counter-Weight [17]	4	200	10	30.0%
Counter-Weight [18]	1000	5000	0.3	20.0%
Magnetic Levitation [10]	/	50	/	1.00%
SEA [24]	14	300(400)	30	5.00%
SEA [25]	5	300(400)	15	4.00%
QZS(torsion bar) [34], [35]	17.3	62.8(100)	1000	4.00%
QZS(magnetic) [31]	400	200(60)	35	0.70%
QZS [36]	1100	800(1000)	836	13.9%
QZS-SDS(our)	**1100**	**12000(800)**	**409**	**4.00%**

1 The SEA/QZS structure sizes of gravity direction are also listed in the table, with form "movement range(structure size)". The dimensions listed refer only to the characteristic structural elements of the QZS mechanism (such as the free length of the spring, MNS spring structure size, etc.), and do not include additional accessories or frame dimensions.

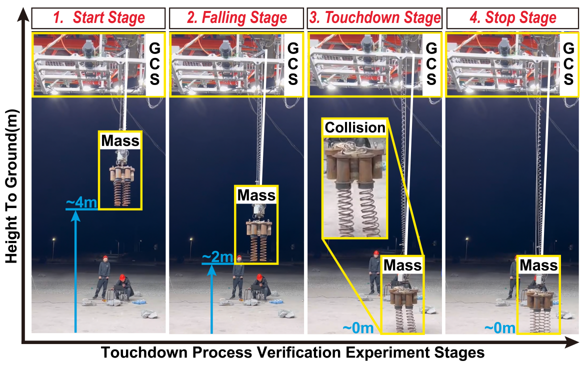

Fig. 2. Experiment stages of touchdown process verification of lander using an equivalent mass.

achieved superior results in terms of simulated motion range, speed, and tension control precision.

The structure of this paper is organized as follows: Section II introduces the application background and the dynamic model of the GCS. Section III presents some basic conclusions of passivity theory and uses them to analyze the input-output characteristics of the GCS, followed by the design and stability analysis of the controller. Section IV describes the results of the simulations and physical experiments. Section V concludes with the specific findings and main contributions of this study.

II. Background and Modeling

A. Problem Formulation

To ensure the stability of an extraterrestrial lander during its touchdown process, it is essential to simulate its operational conditions on Earth. This simulation is conducted to verify the reliability of the engine's ignition and shutdown algorithms post-landing, as well as to assess the adequacy of the landing legs' design in terms of strength and stiffness. The experiment stages for verifying the touchdown process are illustrated in Fig. 2. During the simulation tests of the touchdown process, the load is released from a height of approximately 4m, which can increase to 12m in specific tests, and impacts the ground at a speed between 0.4m/s to 1.1m/s, eventually coming to a stop. The release height (4m–12m) and touchdown velocity range (0.4m/s–1.1m/s) used here are typical for soft-lander touchdown velocity tests [44], [45], [46]. Under ideal controlled conditions, the lander's touchdown velocity should be around 1.0m/s [47], [48]. Throughout this descent, a consistent low-gravity environment must be maintained. The key performance indicator for these tests is the precision of the low-gravity environment during the lander's Stage 3 touchdown process. The outcomes of this stage are crucial for establishing the validity and reliability of the ground verification experiments.

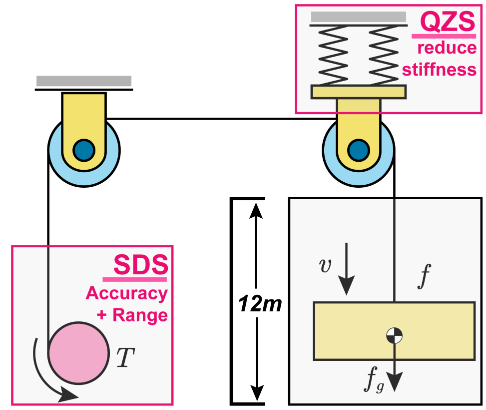

Fig. 3. Simplified schematic of the GCS structure. The QZS reduces endpoint stiffness, while the SDS provides active regulation.

To accurately simulate a low-gravity environment during the landing process, the proposed GCS employs a QZS mechanism to apply force and withstand disturbances. It also integrates a Servo Drive System(SDS) to proactively regulate and minimize compensation force discrepancies. The system's design is depicted in Fig. 4. The QZS is a lever mechanism driven by an adjustable-length spring structure, which ensures parallel connections through a slide rail. By varying the spring stiffness, the QZS outputs constant force with varying magnitudes within a specific range of motion. The springs connect to the base frame via a T-shaped screw rod and to the cable via a flange, which passes through a pulley and links to the QZS lever. By adjusting the length of screw rod, springs' preload length can be adjusted.

The Servo Drive System(SDS) consists of 2 main components: a servo motor and cable-winch structures. The servo motor drives the winch through a reducer to apply a specified force on the cable wound around it. This cable is connected to the lander via a pulley system across the QZS lever. A brake is installed at the end of the SDS winch to rapidly stop the motor shaft, ensuring experimental safety. The GCS can be simplified as the structure shown in Fig. 3, where the SDS directly provides the low-gravity simulation environment for the lander, while the QZS acts to reduce the endpoint stiffness, ensuring that the output force of the SDS remains stable under the strong impact disturbances during touchdown. Furthermore, since the motion range of the GCS is essentially determined by the travel of the SDS motor, this approach effectively extends the limited stroke of the QZS imposed by mechanical constraints. In this study, the GCS is required to provide at least a 12m low-gravity simulation range, whereas the QZS mechanism alone is limited to about 0.9m due to mechanical size restrictions. By introducing the SDS, the operational range of the GCS can be extended beyond 12m.

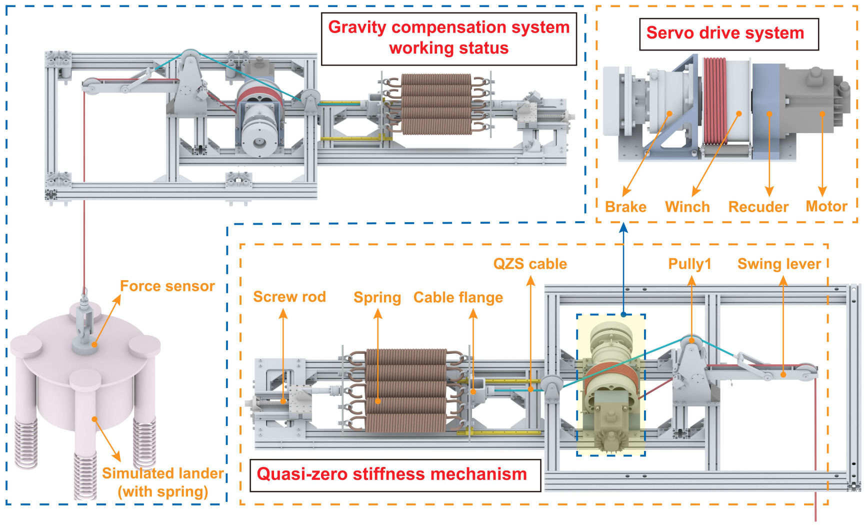

Fig. 4. Structure scheme of the GCS. The GCS is composed of a quasi-zero stiffness mechanism(QZS) and a servo drive system(SDS).

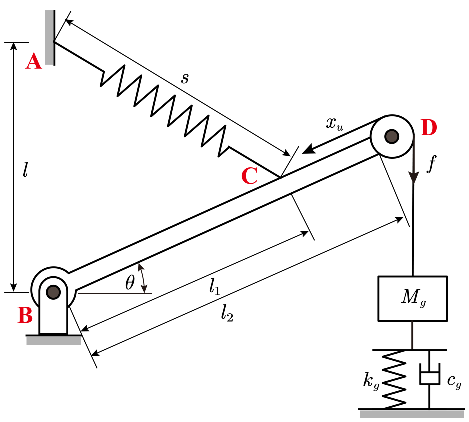

Fig. 5. Schematic model of the QZS.

In summary, the active regulation of the SDS, in combination with the QZS, enables effective low-gravity verification during the lander's touchdown process.

B. Dynamic Model of GCS

1. QZS Dynamic Model: The schematic model of the QZS is shown in Fig. 5, which is simplified as a spring-suspended lever structure. The dynamic model of the QZS is given by (1):

$$\frac{m}{3}l_2^2\ddot{\theta} = -\frac{m}{2}gl_2\cos\theta - T_f - fl_2\cos\theta + k\frac{s-s_0}{s}ll_1\cos\theta \quad (1)$$

When the QZS is in equilibrium, the force balance equation is given by (2) with $s_0 = 0$:

$$f = k\frac{ll_1}{l_2} - \frac{T_f}{l_2\cos\theta} - \frac{mg}{2} \quad (2)$$

By ignoring the frictional force T_f, the force output of the QZS remains constant. In our previous research [36], the QZS is designed to output specified force $f^\star$ with ideal spring stiffness $k^\star = \left(f^\star + mg/2\right) l_2/(ll_1)$. In practical scenarios, several challenges emerge. Firstly, manufacturing variations in spring stiffness ($k = k^\star + \delta k$) lead to discrepancies between the desired force $f^\star$ and the actual force f. Moreover, when the intended compensation force is significant, the rotational friction acting on pivot B becomes noteworthy. These factors collectively contribute to inaccuracies in the QZS's force output. Under these circumstances, the dynamic model of the QZS can be represented as (3).

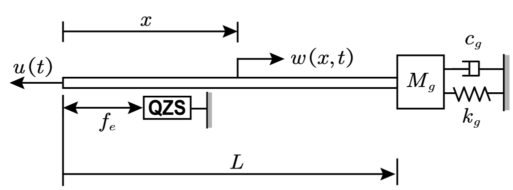

Fig. 6. Schematic model of the cable-mass system.

$$\frac{1}{3}ml_2^2\ddot{\theta} = \left(f^\star - f + \delta k \cdot \frac{ll_1}{l_2}\right) l_2\cos\theta - T_f \quad (3)$$

where:

1) $f_e = f^\star - f$ is the error of target force and actual force.
2) $f_{dk} = \delta kll_1/l_2$ is the force error caused by spring stiffness deviation.

Taken the friction model of lever as Coulomb type as (4).

$$T_f = T_\mu \mathrm{sgn}\dot{\theta} + C_\mu\dot{\theta} \quad (4)$$

Substitute the (4) into (3) yields the model of QZS as (5):

$$\frac{1}{3}ml_2^2\ddot{\theta} = (f_e + f_{dk})\, l_2\cos\theta - \left(T_\mu \mathrm{sgn}\dot{\theta} + C_\mu\dot{\theta}\right) \quad (5)$$

2. Cable-Mass Dynamic Model: For the cable-mass system(CMS), the cable is considered as a continuous elastic medium. A coordinate is established for the cable under the deformation field of the desired tension. Using a string vibration model, the vibration equation of the CMS system is represented by (6), and its structure is shown in Fig. 6.

$$EA\frac{\partial^2 w}{\partial x^2} = \rho\frac{\partial^2 w}{\partial t^2} \quad (6)$$

The boundary conditions of (6) can be expressed as below:

1) $w(0,t) = -u(t) = -(x_u + l_2 \sin\theta)$, which means the cable is constrained by QZS and SDS together, and the constraint force is f_e.
2) $w(L,t)$ is constrained by a spring-mass system.

Applying the assumed mode methods, the vibration equation of CMS can be expressed as (7):

$$w(x,t) = \sum_{i=1}^{N} \phi_i(x) q_i(t) \tag{7}$$

Hence, the kinetic and potential energy of CMS can be expressed as (8):

$$\begin{aligned} T &= \frac{1}{2}\sum_{i=1}^{N}\sum_{j=1}^{N} M_{ij}\dot{q}_i\dot{q}_j + \frac{1}{2}M_g\dot{w}^2(L,t) \\ U &= \frac{1}{2}\sum_{i=1}^{N}\sum_{j=1}^{N} K_{ij}q_iq_j + \frac{1}{2}k_g w^2(L,t) \end{aligned} \tag{8}$$

where:

$$\begin{aligned} M_{ij} &= \int_0^L \rho A \phi_i(x)\phi_j(x)\,\mathrm{d}x \\ K_{ij} &= \int_0^L \rho A \phi_i'(x)\phi_j'(x)\,\mathrm{d}x \end{aligned} \tag{9}$$

Take $\boldsymbol{q} = [q_1, \ldots, q_N]^T$ as the state variable of CMS, the virtual work $\boldsymbol{Q}\cdot\delta\boldsymbol{q}$ can be expressed as (10):

$$\boldsymbol{Q}\cdot\delta\boldsymbol{q} = -c_g\dot{w}(L,t)\delta w(L,t) + f_e\delta w(0,t) \tag{10}$$

Applying the generalized Hamiltonian principle, the dynamic equation of CMS can be expressed as (11):

$$\int_{t_1}^{t_2} (\delta\mathcal{L} - \boldsymbol{Q}\cdot\delta\boldsymbol{q})\,\mathrm{d}t = 0 \tag{11}$$

where the lagrangian is $\mathcal{L} = T - U$. Substitute (8) into (11) yields the dynamic equation of CMS as (12):

$$\boldsymbol{M}\ddot{\boldsymbol{q}} + \boldsymbol{C}\dot{\boldsymbol{q}} + \boldsymbol{K}\boldsymbol{q} = \boldsymbol{F} \tag{12}$$

where:

$$\begin{aligned} \boldsymbol{M} &= \begin{bmatrix} M_{11} & \ldots & M_{1N} \\ \vdots & M_{ij} & \vdots \\ M_{N1} & \ldots & M_{NN} \end{bmatrix} + M_g\boldsymbol{\phi}_L\boldsymbol{\phi}_L^T \\ \boldsymbol{C} &= c_g\boldsymbol{\phi}_L\boldsymbol{\phi}_L^T \\ \boldsymbol{K} &= \begin{bmatrix} K_{11} & \ldots & K_{1N} \\ \vdots & K_{ij} & \vdots \\ K_{N1} & \ldots & K_{NN} \end{bmatrix} + k_g\boldsymbol{\phi}_L\boldsymbol{\phi}_L^T \\ \boldsymbol{F} &= \boldsymbol{\phi}_0 f_e \end{aligned} \tag{13}$$

$$\begin{aligned} \boldsymbol{q} &= [q_1(t), \ldots, q_N(t)]^T \\ \boldsymbol{\phi}_L &= [\phi_1(L), \ldots, \phi_N(L)]^T \\ \boldsymbol{\phi}_0 &= [\phi_1(0), \ldots, \phi_N(0)]^T \end{aligned} \tag{14}$$

To solve the constraint force f_e at $x = 0$, transform the constraint equation at $x = 0$ as (15):

$$\boldsymbol{\Phi}(\boldsymbol{q},t) = \boldsymbol{\phi}_0^T\boldsymbol{q} + u(t) = 0 \tag{15}$$

where $u(t) = x_u + l_2\sin\theta$ is the displacement constraint. Notice that the boundary constraint is holonomic, the constraint force can be solved by the Lagrange multiplier method [49] as (16):

$$\begin{bmatrix} \boldsymbol{M} & \boldsymbol{\phi}_0 \\ \boldsymbol{\phi}_0^T & 0 \end{bmatrix}\begin{bmatrix} \ddot{\boldsymbol{q}} \\ -f_e \end{bmatrix} = \begin{bmatrix} -\boldsymbol{C}\dot{\boldsymbol{q}} - \boldsymbol{K}\boldsymbol{q} \\ -\ddot{u} \end{bmatrix} \tag{16}$$

Moreover, because the matrix $\boldsymbol{M}$ is full rank, then $\ddot{\boldsymbol{q}}$ can be expressed as (17):

$$\ddot{\boldsymbol{q}} = \boldsymbol{M}^{-1}\boldsymbol{\phi}_0 f_e - \boldsymbol{M}^{-1}(\boldsymbol{C}\dot{\boldsymbol{q}} + \boldsymbol{K}\boldsymbol{q}) \tag{17}$$

Substitute (17) into constraint equation (16) yields (18):

$$f_e = \frac{-\ddot{u} + \boldsymbol{\phi}_0^T\boldsymbol{M}^{-1}(\boldsymbol{C}\dot{\boldsymbol{q}} + \boldsymbol{K}\boldsymbol{q})}{\boldsymbol{\phi}_0^T\boldsymbol{M}^{-1}\boldsymbol{\phi}_0} \tag{18}$$

Hence the constraint force f_e can be solved by extended state space model and the internal states can be updated via boundary constraint $u(t) = x_u + l_2\sin\theta$.

III. System Analysis and Controller Design

A. Basic Knowledge of Passivity Theory

In this section, some main results of passivity theory are introduced [42], [43].

Considering following dynamic system (19):

$$\begin{aligned} \frac{\mathrm{d}}{\mathrm{d}t}\boldsymbol{x}(t) &= \boldsymbol{f}(\boldsymbol{x}(t), \boldsymbol{u}(t)) \quad && \boldsymbol{f}(\boldsymbol{0},\boldsymbol{0}) = \boldsymbol{0} \\ \boldsymbol{y}(t) &= \boldsymbol{h}(\boldsymbol{x}(t), \boldsymbol{u}(t)) \quad && \boldsymbol{h}(\boldsymbol{0},\boldsymbol{0}) = \boldsymbol{0} \end{aligned} \tag{19}$$

where $\boldsymbol{x}(t) \in \mathbb{R}^n$, $\boldsymbol{u}(t) \in \mathbb{R}^m$, $\boldsymbol{y}(t) \in \mathbb{R}^p$, with $\boldsymbol{f}: \mathbb{R}^n \times \mathbb{R}^m \to \mathbb{R}^n$ is a continuous differentiable map. The definition of passivity is introduced through the system's input-output characteristics, with the core concept being a scalar-valued supply rate $s(\boldsymbol{u}, \boldsymbol{y})$ used to constrain the system's "energy".

Definition 1: If a map $V : \mathbb{R}^n \to \mathbb{R}$ satisfies $V(\boldsymbol{0}) = 0, V(\boldsymbol{x}) \geqslant 0, \forall \boldsymbol{x}$, and the following inequality holds:

$$V(\boldsymbol{x}(\tau)) - V(\boldsymbol{x}(0)) \leqslant \int_0^\tau s(\boldsymbol{u}(t), \boldsymbol{y}(t))\,\mathrm{d}t \tag{20}$$

for any input signal $\boldsymbol{u}(t)$ and time $\tau \geqslant 0$, the system is dissipative. When $s(\boldsymbol{u},\boldsymbol{y}) = \boldsymbol{u}^T\boldsymbol{y}$, the system is passive. When $s(\boldsymbol{u},\boldsymbol{y}) = \boldsymbol{u}^T\boldsymbol{y} - \varepsilon\|\boldsymbol{y}\|^2$ with $\varepsilon > 0$, the system is output strictly passive. $V(\cdot)$ serves as the storage function for the system. If a class of systems exhibits passive characteristics, it becomes convenient to assess the Lyapunov stability of their interconnected structure. We first give the passivity criteria for system which is affine in the input u.

Theorem 1 (passivity criteria for system which is affine in input u:) For an affine system (21):

$$\begin{aligned} \frac{\mathrm{d}\boldsymbol{x}}{\mathrm{d}t} &= \boldsymbol{f}(\boldsymbol{x}) + \boldsymbol{g}(\boldsymbol{x})u \\ y &= h(\boldsymbol{x}) \end{aligned} \tag{21}$$

The necessary and sufficient condition for a system to be passive is the existence of a storage function V that ensures (22), where $\nabla V = \partial V/\partial\boldsymbol{x}$.

$$\begin{cases} \nabla V(\boldsymbol{x})^T\boldsymbol{f}(\boldsymbol{x}) \leqslant 0, \forall\boldsymbol{x} \in \mathbb{R}^n \\ \nabla V(\boldsymbol{x})^T\boldsymbol{g}(\boldsymbol{x}) = h(\boldsymbol{x}), \forall\boldsymbol{x} \in \mathbb{R}^n \end{cases} \tag{22}$$

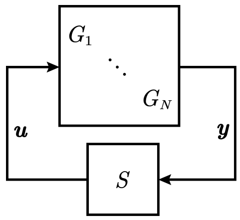

Fig. 7. Interconnection structure of multiple passive system.

The previously mentioned theorem 1 can be utilized to ascertain whether affine systems are passive. In structures where multiple passive systems are interconnected, the subsequent theorem can be employed to confirm their Lyapunov stability.

Theorem 2 (criteria of Lyapunov stability for multi-system interconnected structure:) Consider multiple system $G_i, i = 1, \ldots, N$ as (2):

$$\frac{\mathrm{d}}{\mathrm{d}t}\boldsymbol{x}_i(t) = \boldsymbol{f}_i(\boldsymbol{x}_i(t), \boldsymbol{u}_i(t))$$
$$\boldsymbol{y}_i(t) = \boldsymbol{h}_i(\boldsymbol{x}_i(t), \boldsymbol{u}_i(t)) \tag{23}$$

The interconnection structure is shown as Fig. 7. The composite input vector $\boldsymbol{u} = \left[\boldsymbol{u}_1^T, \ldots, \boldsymbol{u}_N^T\right]^T$ and the output vector is $\boldsymbol{y} = \left[\boldsymbol{y}_1^T, \ldots, \boldsymbol{y}_N^T\right]^T$, where $\boldsymbol{u} = \boldsymbol{S}\boldsymbol{y}$.

Each subsystem is (output strict) passive, hence the supply rate of system G_i can be expressed as (24):

$$s_i\left(\boldsymbol{u}_i, \boldsymbol{y}_i\right) = \begin{bmatrix} \boldsymbol{u}_i \\ \boldsymbol{y}_i \end{bmatrix}^T \boldsymbol{X}_i \begin{bmatrix} \boldsymbol{u}_i \\ \boldsymbol{y}_i \end{bmatrix} \tag{24}$$

where:

$$\boldsymbol{X}_i = \begin{bmatrix} \boldsymbol{0} & \frac{1}{2}\boldsymbol{I} \\ \frac{1}{2}\boldsymbol{I} & -\varepsilon_i\boldsymbol{I} \end{bmatrix}, \varepsilon_i \geqslant 0 \tag{25}$$

Then the following theorem exists: If the entire system of interconnected subsystems is Lyapunov stable, its Lyapunov function can be represented as a linear combination of the storage functions of each subsystem (26):

$$V = p_1 V_1(\boldsymbol{x}_1) + \ldots + p_N V_N(\boldsymbol{x}_N), p_i \geqslant 0, i = 1, \ldots, N \tag{26}$$

Which should meet (27):

$$\boldsymbol{P}(\boldsymbol{S} - \boldsymbol{E}) + (\boldsymbol{S} - \boldsymbol{E})^T \boldsymbol{P} \leqslant \boldsymbol{0} \tag{27}$$

where $\boldsymbol{P} = \mathrm{diag}(p_1, \ldots, p_N)$, $\boldsymbol{E} = \mathrm{diag}(\varepsilon_1, \ldots, \varepsilon_N)$.

According to theorem 2, it can be readily inferred that when two passive systems are interconnected via feedback, the compound system is Lyapunov stable if at least one of the systems is output strictly passive. Furthermore, additional analysis leads to the well-known Small Gain Theorem.

B. QZS and CMS Passivity Analysis

The feedback control loop structure of the GCS is depicted in Fig. 8. The feedback interconnection between the QZS and the Cable-Mass System(CMS) illustrates a scheme where only the QZS is utilized for force compensation. Incorporating a controller into this structure forms the complete feedback interconnection system examined in this paper.We first apply passivity theory to analyze the shortcomings of the scheme where only the QZS and CMS are interconnected to regulate the output force.

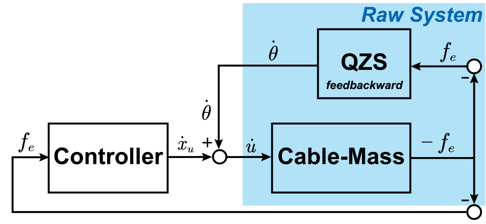

Fig. 8. Control loop structure of the GCS.

1. QZS Passivity Analysis: The dynamic model of QZS can be expressed as (5), the input and output signal of QZS in the feedback loop is $u_{\mathrm{QZS}} = f_e$ and $y_{\mathrm{QZS}} = \mathrm{d}(l_2 \sin\theta)/\mathrm{d}t = l_2 \cos\theta\dot{\theta}$ respectively. Denote $x_1 = \theta$, $x_2 = \dot{\theta}$, $\boldsymbol{x} = [x_1, x_2]^T$, the dynamic model of QZS can be further simplified as an affine system (28):

$$\frac{\mathrm{d}x_1}{\mathrm{d}t} = x_2$$
$$\frac{\mathrm{d}x_2}{\mathrm{d}t} = f_1(\boldsymbol{x}) + g_1(\boldsymbol{x}) f_e \tag{28}$$

where:

$$f_1(\boldsymbol{x}) = \frac{3}{ml_2^2}\left(f_{dk} l_2 \cos x_1 - T_\mu \mathrm{sgn} x_2 - C_\mu x_2\right)$$
$$g_1(\boldsymbol{x}) = \frac{3}{ml_2}\cos x_1 \tag{29}$$

Accodring to theorem 1, the necessary and sufficient condition for QZS to be passive is that there exists a storage function $V(\boldsymbol{x})$ which ensure (22), hence:

$$\frac{\partial V}{\partial x_2} g_1(x_1) = (l_2 \cos x_1) x_2 \tag{30}$$

which means that (31) should holds:

$$V = V_1(x_1) + \frac{1}{6} m l_2^2 x_2^2 \tag{31}$$

Substitute (31) into (22) yields (32):

$$\frac{\mathrm{d}V_1}{\mathrm{d}x_1} x_2 + \frac{1}{3} m l_2^2 x_2 \cdot f_1(x_1, x_2) \leqslant 0 \quad \forall \boldsymbol{x} \in \mathbb{R}^2 \tag{32}$$

Substitute (29) into (32) yields (33):

$$x_2 \frac{\mathrm{d}}{\mathrm{d}x_1}\tilde{V}_1(x_1) \leqslant T_\mu \|x_2\| + C_\mu x_2^2 \quad \forall \boldsymbol{x} \in \mathbb{R}^2 \tag{33}$$

where $\tilde{V}_1(x_1) = V_1(x_1) + f_{dk} l_2 \sin(x_1)$. Because $C_\mu \geqslant 0, T_\mu \geqslant 0$, (33) is equivalent to (34).

$$\left\| \frac{\mathrm{d}}{\mathrm{d}x_1}\tilde{V}_1(x_1) \right\| \leqslant T_\mu \tag{34}$$

This implies that $\tilde{V}_1(x_1)$ is Lipschitz continuous. Take $\mathrm{d}\tilde{V}_1(x_1)/\mathrm{d}x_1 \equiv 0$, which makes the QZS passive, thereby validating (35).

$$V = \frac{1}{6} m l_2^2 \dot{\theta}^2 - f_{dk} l_2 \sin\theta \tag{35}$$

Take time derivative to V yields (36):

$$\dot{V} = \frac{1}{3} m l_2^2 \dot{\theta}\ddot{\theta} - f_{dk} l_2 \cos\theta\dot{\theta}$$

$$
\begin{aligned}
&= f_e l_2 \dot{\theta} \cos\theta - T_\mu \left\|\dot{\theta}\right\| - C_\mu \dot{\theta}^2 \\
&= u_{\mathrm{QZS}}^T y_{\mathrm{QZS}} - T_\mu \left\|\dot{\theta}\right\| - C_\mu \dot{\theta}^2 \\
&\leqslant u_{\mathrm{QZS}}^T y_{\mathrm{QZS}} - \gamma^2 y^2
\end{aligned} \tag{36}
$$

where $\gamma^2 = C_\mu / l_2^2$. In summary, the analysis presented demonstrates that the QZS system is output strict passive.

Remark 1 (35) also indicates that if the QZS is passive, the storage function V must be non-negative. This implies that when $f_{dk} = 0$, meaning there are no spring stiffness deviations, the QZS is always passive. If $f_{dk} \neq 0$, choosing $f_{dk} < 0$ ensures the passivity of the QZS. Since the lever angle θ is restricted to be positive ($\theta > 0$) by the mechanism, the storage function $V \geqslant 0$ within the working range. Furthermore, (34) indicates that under certain conditions, the passivity of the QZS can be ensured even when $f_{dk} > 0$. For instance, consider $\tilde{V}_1(x_1) = T_\mu \sin(x_1)$. If $T_\mu \geqslant f_{dk} l_2$, then $V = 1/6\, m l_2^2 \dot{\theta}^2 + \left(T_\mu - f_{dk} l_2\right) \sin\theta$ remains a suitable energy storage function. This implies that in practical scenarios, if the friction T_μ is sufficiently large, the system remains passive despite the presence of spring stiffness deviation $f_{dk} > 0$.

Remark 2 (35) reveals the passivity property of the QZS, a conclusion that can be generalized to all similar QZS structures. The core reason lies in the fact that these QZS systems require a constant potential energy to maintain quasi-zero stiffness. Consequently, when deriving the system dynamics model using the Lagrange principle, it contains only kinetic energy terms, resulting in a similar equation structure.

2. CMS Passivity Analysis: The dynamic model of the CMS can be expressed as (16). Denote $\boldsymbol{X} = \left[\boldsymbol{q}, \dot{\boldsymbol{q}}\right]^T$, and define the CMS input-output signals as $u_{\mathrm{CMS}} = l_2 \cos\theta\dot{\theta} + \dot{x}_u$ and $y_{\mathrm{CMS}} = -f_e$ to maintain physical significance. Assume the LTI system has a quadratic storage function V as given in (37):

$$
V = \frac{1}{2}\boldsymbol{q}^T \boldsymbol{P}_1 \boldsymbol{q} + \frac{1}{2}\dot{\boldsymbol{q}}^T \boldsymbol{P}_2 \dot{\boldsymbol{q}} \tag{37}
$$

where $\boldsymbol{P}_1, \boldsymbol{P}_2$ are positive semi-definite real symmetric matrix. If CMS is passive, then according to definition 1, (38) should holds.

$$
\dot{\boldsymbol{q}}^T \boldsymbol{P}_1 \boldsymbol{q} + \ddot{\boldsymbol{q}}^T \boldsymbol{P}_2 \dot{\boldsymbol{q}} \leqslant \boldsymbol{\phi}_0^T \dot{\boldsymbol{q}} f_e \tag{38}
$$

Substitute (17) into (38) yields (39):

$$
\dot{\boldsymbol{q}}^T \left(\boldsymbol{P}_1 - \tilde{\boldsymbol{P}}_2 \boldsymbol{K}\right) \boldsymbol{q} + \dot{\boldsymbol{q}}^T \left(\tilde{\boldsymbol{P}}_2 - \boldsymbol{I}\right) \boldsymbol{\phi}_0 f_e \leqslant \dot{\boldsymbol{q}}^T \tilde{\boldsymbol{P}}_2 \boldsymbol{C} \dot{\boldsymbol{q}} \tag{39}
$$

where $\tilde{\boldsymbol{P}}_2 = \boldsymbol{P}_2 \boldsymbol{M}^{-1}$. Notice that f_e is affine to constraint $\ddot{u}$ according to (18), (39) can be further simplified as (40):

$$
\begin{cases}
\dot{\boldsymbol{q}}^T \left(\tilde{\boldsymbol{P}}_2 - \boldsymbol{I}\right) \boldsymbol{\phi}_0 = 0 \\
\boldsymbol{P}_1 - \tilde{\boldsymbol{P}}_2 \boldsymbol{K} = 0
\end{cases} \tag{40}
$$

Hence (41) holds:

$$
\begin{cases}
\boldsymbol{P}_2 = \boldsymbol{M} \\
\boldsymbol{P}_1 = \boldsymbol{K}
\end{cases} \tag{41}
$$

Substitute (41) into (37) yields (42):

$$
V = \frac{1}{2}\boldsymbol{q}^T \boldsymbol{K} \boldsymbol{q} + \frac{1}{2}\dot{\boldsymbol{q}}^T \boldsymbol{M} \dot{\boldsymbol{q}} \tag{42}
$$

Take time derivative of V and substitute $\boldsymbol{\phi}_0^T \dot{\boldsymbol{q}} = -u_{\mathrm{CMS}}$ into it returns (43):

$$
\begin{aligned}
\dot{V} &= \boldsymbol{q}^T \boldsymbol{K} \dot{\boldsymbol{q}} + \dot{\boldsymbol{q}}^T \boldsymbol{M} \ddot{\boldsymbol{q}} \\
&= \dot{\boldsymbol{q}}^T \boldsymbol{F} - \dot{\boldsymbol{q}}^T \boldsymbol{C} \dot{\boldsymbol{q}} \\
&= \dot{\boldsymbol{q}}^T \boldsymbol{\phi}_0 f_e - \dot{\boldsymbol{q}}^T \boldsymbol{C} \dot{\boldsymbol{q}} \\
&= u_{\mathrm{CMS}}^T y_{\mathrm{CMS}} - \dot{\boldsymbol{q}}^T \boldsymbol{C} \dot{\boldsymbol{q}} \\
&\leq u_{\mathrm{CMS}}^T y_{\mathrm{CMS}}
\end{aligned} \tag{43}
$$

Which suggests that CMS is passive.

3. QZS and CMS Control Error Analysis: Without incorporating an external control system(i.e. SDS), the QZS and CMS systems are interconnected through negative feedback. According to theorem 2, since the QZS system is output strictly passive and the CMS system is passive, their feedback interconnection system is globally asymptotically stable. A suitable candidate Lyapunov function for this system can be considered as follows:

$$
V = \frac{1}{6} m l_2^2 \dot{\theta}^2 - f_{dk} l_2 \sin\theta + \frac{1}{2}\dot{\boldsymbol{q}}^T \boldsymbol{M} \dot{\boldsymbol{q}} + \frac{1}{2}\boldsymbol{q}^T \boldsymbol{K} \boldsymbol{q} \tag{44}
$$

Take time derivative of (44) yields (45):

$$
\dot{V} = -T_\mu \left\|\dot{\theta}\right\| - C_\mu \dot{\theta}^2 - \dot{\boldsymbol{q}}^T \boldsymbol{C} \dot{\boldsymbol{q}} \leqslant 0 \tag{45}
$$

Applying the LaSalle Invariance Principle, QZS and CMS interconnected system is globally asymptotically stable.

However, the aforementioned system faces a fundamental issue: the equilibrium region does not contains the point where $f_e = 0$. Analyzing the stability region of the interconnected system reveals that it satisfies the following condition:

$$
\dot{\theta} = 0, \dot{\boldsymbol{q}} = 0 \tag{46}
$$

Substitute (46) into (18) yields (47):

$$
f_e = \frac{\boldsymbol{\phi}_0^T \boldsymbol{M}^{-1} \boldsymbol{K} \boldsymbol{q}}{\boldsymbol{\phi}_0^T \boldsymbol{M}^{-1} \boldsymbol{\phi}_0} \tag{47}
$$

Moreover, substitute (46) into (5) yields (48):

$$
0 = \left(f_e + f_{dk}\right) l_2 \cos\theta \tag{48}
$$

Which means that f_e will asymptotically converge to $-f_{dk}$.

Remark 3 The QZS friction model utilizes a Coulomb model instead of a state-based model like the LuGre model, which can estimate static friction. This results in $\dot{\theta} = 0 \Longrightarrow T_f = 0$. However, in reality, rotational friction T_f is non-zero when $\dot{\theta} = 0$, causing higher compensation force error in the equilibrium region. This issue can be addressed by integrating an external control system, such as the SDS, to compensate for the friction force.

C. SDS Controller Design

As previously mentioned, relying solely on the feedback interconnection between the QZS and CMS systems ensures that the overall system asymptotically converges to an equilibrium point where $f_e = -f_{dk}$, significant force deviations exist in practical applications. To address this issue, we introduce a new controller that meets two main criteria: first, it must ensure that the complete system, including the new controller, remains globally asymptotically stable; second, it must guarantee that the force error $f_e = 0$ at the system's equilibrium region.

As the Fig. 8 depicts, denote the QZS, CMS and controller as follows:

1) Subsystem1: QZS with input-output map $f_e \to l_2 \cos\theta\dot{\theta}$
2) Subsystem2: CMS with input-output map $l_2 \cos\theta\dot{\theta} + \dot{x}_u \to -f_e$
3) Subsystem3: Controller with input-output map $f_e \to \dot{x}_u$

The feedback interconnection matrix $\boldsymbol{S}$ is (49).

$$\boldsymbol{S} = \begin{bmatrix} 0 & -1 & 0 \\ 1 & 0 & 1 \\ 0 & -1 & 0 \end{bmatrix} \tag{49}$$

Accodring to theorem 2, the necessary and sufficient condition for the interconnected system to be globally asymptotically stable is equivalent to (50):

$$\begin{bmatrix} -2\varepsilon_1 p_1 & -p_1 + p_2 & 0 \\ -p_1 + p_2 & -2\varepsilon_2 p_2 & p_2 - p_3 \\ 0 & p_2 - p_3 & -2\varepsilon_3 p_3 \end{bmatrix} \leqslant 0 \tag{50}$$

Take matrix $\boldsymbol{P} = \mathrm{diag}\,(1, 1, 1)$ into (50) yields (51):

$$\begin{bmatrix} \varepsilon_1 & & \\ & \varepsilon_2 & \\ & & \varepsilon_3 \end{bmatrix} \geqslant 0 \tag{51}$$

Because QZS and CMS system is passive, the globally asymptotically stablility of composite system is met by choosing $\varepsilon_3 \geqslant 0$, which means that the SDS controller is passive. Additionally, the selection of SDS controller should ensure that the force error $f_e = 0$ in the equilibrium region. Among the various structures of passive controllers, fuzzy controllers are widely employed in engineering practice due to their robustness to parameter variations [50], [51], [52], [53]. Therefore, in this study, we exemplify a fuzzy PID controller for simulation and experimental purposes.

Remark 4 We have demonstrated that as long as the SDS controller is passive and its storage function's stability region encompasses the desired point, this class of controllers is applicable for designing the GCS. The selection of a fuzzy PID controller in this context is made for the convenience of experimental implementation.

Take the SDS fuzzy controller as (52):

$$\dot{x}_u = k_p f_e + k_d \dot{f}_e + h\,(f_e, \dot{x}_u) \tag{52}$$

where $h(f_e, \dot{x}_u)$ is the fuzzy controller. The two inputs of the fuzzy controller are the force error f_e and the movement velocity $\dot{x}_u$, and the output is the regulation signal. Based on prior knowledge, f_e is divided into 3 fuzzy subsets, which are labeled as NF, MF and PF. The fuzzy subsets of touchdown velocity are also defined in terms of 3 language variables, noted as LV, MV and HV. The output compensation velocity is divided into 6 subsets as NHU, NMU, NLU, PLU, PMU and PHU. The specific membership functions of fuzzy subsets determine the inference results of fuzzy controller as Fig. 9 and Fig. 10. Trapmf membership functions are selected for the force error and touchdown velocity input, while the trimf membership functions are chosen for the compensation velocity output. The fuzzy inference rules are listed in Table II

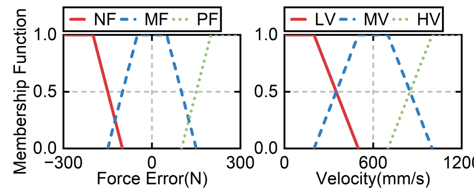

Fig. 9. Input membership functions of the fuzzy controller.

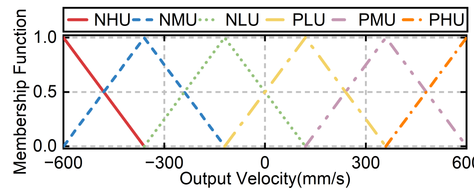

Fig. 10. Output membership functions of the fuzzy controller.

TABLE II
INFERENCE RULES OF THE FUZZY CONTROLLER

Input		Output
Force Error	Touchdown Velocity	Compensation Velocity
NF	LV	NLU
NF	MV	NMU
NF	HV	NHU
PF	LV	PLU
PF	MV	PMU
PF	HV	PHU

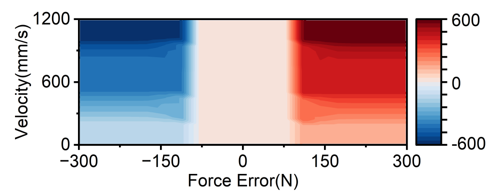

Fig. 11. Input-Output mapping surface of the fuzzy controller.

and the output versus input variables of the fuzzy controller is shown in Fig. 11. The logical operators follows the Mamdani style, where "And" operator is replaced by "Min", "Or" operator is replaced by "Max". The implication method is chosen as "Min", the aggregation method is chosen as "Max" and the defuzzification method is chosen as "centroid".

Take the candidate Lyapunov function of fuzzy control system as (53):

$$V = \frac{1}{2} k_d f_e^2 \tag{53}$$

Take time derivative of V yields (54):

$$\begin{aligned} \dot{V} &= k_d \dot{f}_e f_e \\ &= \dot{x}_u f_e - k_p f_e^2 - f_e h\,(f_e, \dot{x}_u) \end{aligned} \tag{54}$$

According to Fig. 11, the fuzzy controller satisfies $f_e h\,(f_e, \dot{x}_u) \geqslant 0$, which ensures the passivity of the fuzzy controller. Meanwhile, with the existence of the fuzzy controller, the equilibrium region of the GCS system is expanded to include the point where $f_e = 0$. By adjusting the fuzzy membership functions and inference rules, the energy dissipation rate of the system can be further enlarged with the whole

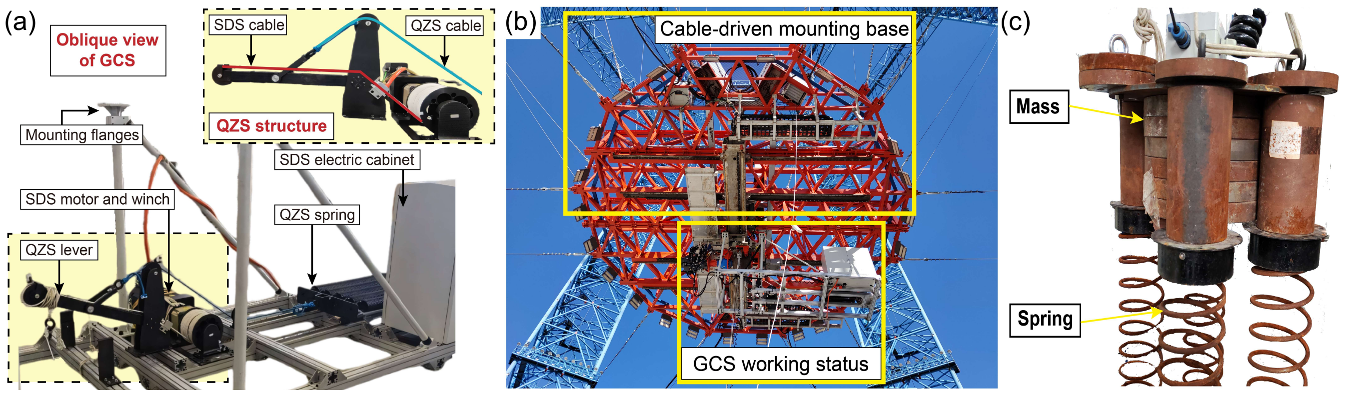

Fig. 12. GCS structure overview. (a)The GCS hardware overview. (b)The working status of the GCS. (c)Simulated lander used in the experiment. The rated mass is 420kg and the rated spring stiffness is 11.2N/mm.

TABLE III
PROTOTYPE COMPONENTS MANUFACTURERS

Component	Characteristics
SDS Motor	Rated torque 93Nm, speed 2000rpm
SDS Driver	Rated voltage 3x400V AC, current 104A
Reducer	Gear ratio 1:4, inertia 24kgcm^2
Spring	Stiffness 3.95N/mm×5, external diameter 97mm
Control PLC	Control loop 1kHz, CPU Intel Atom® 1.75 GHz
Force Sensor	Sensitivity 0.5mV/V, relative linearity 0.5%
Force Acquisitor	Sample rate 1kHz, resolution 24bit

energy unchanged to increase the convergence speed of the system.

By incorporating the fuzzy controller (52) into the GCS system, and take the matrix $\boldsymbol{P} = \text{diag}(1, 1, 1)$, the candidate Lyapunov function of interconnected system is (55):

$$V = \frac{1}{6}ml_2^2\dot{\theta}^2 - f_{dk}l_2\sin\theta + \frac{1}{2}\dot{\boldsymbol{q}}^T\boldsymbol{M}\dot{\boldsymbol{q}} + \frac{1}{2}\boldsymbol{q}^T\boldsymbol{K}\boldsymbol{q} + \frac{1}{2}k_d f_e^2 \quad (55)$$

Take time derivative of V yields (56):

$$\dot{V} = -T_\mu \left\|\dot{\theta}\right\| - C_\mu\dot{\theta}^2 - \dot{\boldsymbol{q}}^T\boldsymbol{C}\dot{\boldsymbol{q}} - k_p f_e^2 - f_e h\left(f_e, \dot{x}_u\right) \leqslant 0 \quad (56)$$

It is clear that the interconnected system is globally asymptotically stable. Moreover, the equilibrium region of the system is expanded to include the point where $f_e = 0$. The fuzzy controller ensures that the force error f_e converges to zero in the equilibrium region, which is beneficial for practical applications.

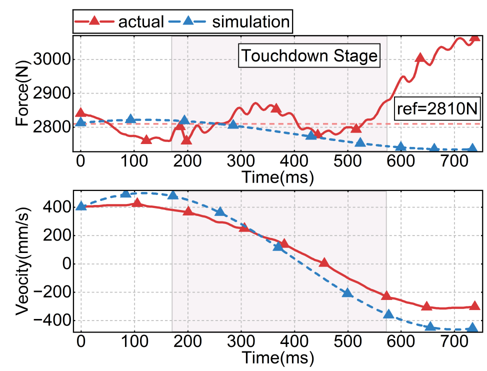

Fig. 13. Touchdown experiment in 0.4m/s velocity.

TABLE IV
EXPERIMENT GROUPS AND RESULTS

Group	Velocity (m/s)	Target Force (N)	Stiffness (N/mm)	Maximum Force Error (N)
1(Fig.13)	0.4	2813	11.2	53.67(1.9%)
2(Fig.14)	0.6	2813	11.2	66.64(2.4%)
3(Fig.15)	0.8	2813	11.2	110.16(3.9%)
4(Fig.16)	1.1	2813	11.2	111.99(4.0%)
5(Fig.17)	0.4, 0.6, 0.8, 1.1	2813	6.4	-50.42, -45.68, 41.95, 14.42 (5.8%, 4.6%, 4.3%, 5.2%)
6(Fig.18)	0.4, 0.6, 0.8, 1.1	2813	11.2	53.67, 66.64, 110.16, 111.99 (1.9%, 2.4%, 3.9%, 4.0%)
7(Fig.19)	0.4,0.6, 0.8, 1.1	2813	16	14.38, 78.57, 110.67, 119.63 (0.5%, 2.8%, 3.9%, 4.2%)
8(Fig.20)	0.4, 0.6, 0.8, 1.1	3341	11.2	14.02, 85.79, 150.0, 162.15 (0.4%, 2.5%, 4.5%, 4.8%)

IV. EXPERIMENTS

A. Experimental Setup

Based on previous analysis, a physical prototype of the GCS has been constructed, as depicted in Fig. 12. The cable-driven mounting base remains stationary when the GCS begins operation. The simulated lander comprises an adjustable mass and springs, designed to mimic the stiffness characteristics of the lander's legs.

The parameters of the main components are listed in Table III. In the experiment, the lander initiates its descent from a height of 4-12m above the ground with velocities ranging from 0.4 to 1.1m/s. Due to the stiffness of the lander's legs, the touchdown process will extend over a certain duration. Throughout this process, a 5/6 acceleration of Earth gravity compensation is required. The maximum mass of the lander is 420kg, hence the maximum compensation force is 3430N.

To demonstrate the effectiveness of the control law, a series of experiments are proposed under various conditions. The experiment groups and results are listed in Table IV. Initially, experiments are conducted at different touchdown velocities(0.4 to 1.1m/s) and stiffness levels(6.4 to 16.0N/mm). Next, to show the versatility of the proposed method, tests with higher target forces are performed by replacing the QZS springs, thus validating the method's effectiveness under various payload conditions. Finally, compared to tests using

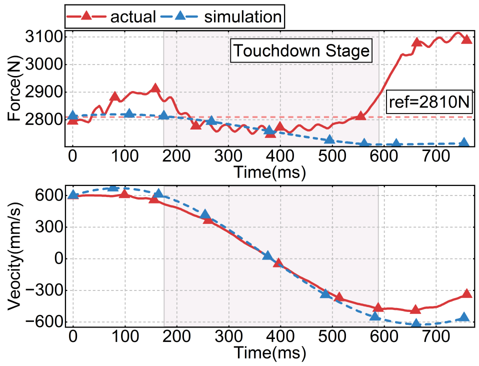

Fig. 14. Touchdown experiment in 0.6m/s velocity.

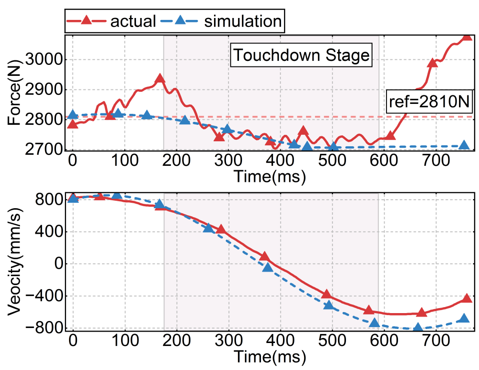

Fig. 15. Touchdown experiment in 0.8m/s velocity.

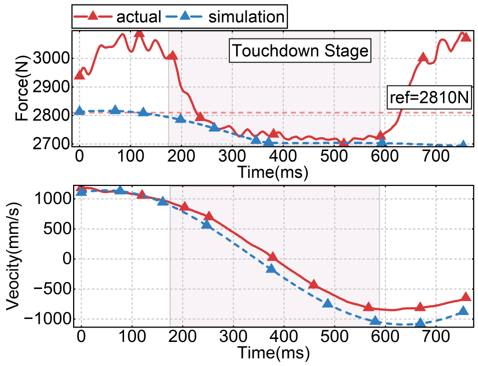

Fig. 16. Touchdown experiment in 1.1m/s velocity.

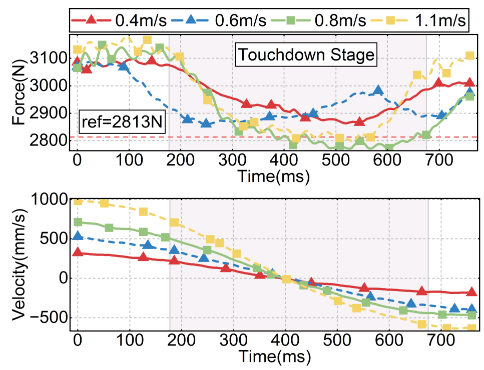

Fig. 17. Touchdown experiment with 6.4N/mm contact stiffness. Results of velocity 0.4m/s-1.1m/s are shown.

only the QZS and SDS, the significance of the proposed method for high-precision low-gravity simulation is confirmed.

B. Variable Touchdown Velocities Experiments

The touchdown experiments conducted at varying velocities are depicted in Fig. 13 to Fig. 16. In all 4 experiments, the target compensation force is set at 2813N, and the contact stiffness between the lander and the ground is fixed at 11.2N/mm. Throughout the touchdown process, the controller functions to mitigate the force reduction caused by impact, with its operation lasting approximately 400ms.

The experimental results indicate that an increase in the lander's touchdown velocity leads to a higher deviation in the compensation force during the touchdown stage. For instance, when the touchdown velocity is 0.4 m/s, the maximum deviation of the GCS compensating force is 53.67 N, corresponding to a force compensation error of 1.9%. Conversely, at a velocity of 1.1 m/s, this deviation increased to 111.99 N, resulting in a 4.0% error. Compare to the simulation results, both the output force and velocity demonstrate consistency.

It is noteworthy that in the actual experimental results, force curves fluctuate both before and after the touchdown stage. Prior to entering the touchdown stage, the fluctuation occurs due to the limited output response bandwidth of the SDS motor in the physical world. As the touchdown velocity increases, the feedforward force compensation error applied before ground contact gradually intensifies. In simulations, this fluctuation is absent since the motor's internal torque regulation limitations are not considered. Following the touchdown stage, the GCS controller stops operating and actively increases the motor's output force to maintain a minimal ground contact force for the lander. Despite the fluctuation in compensation force around the touchdown stage in actual experiments, the main objective is to preserve the accuracy of the low-gravity simulation environment for the lander during this critical phase. Thus, this study primarily assesses the accuracy of the GCS compensation force output during the touchdown stage.

In conclusion, both the simulation and experimental results across various ground touchdown velocities affirm the robustness of the proposed controller against variations in touchdown velocity. Furthermore, the GCS can maintain a control error of 4% even at a velocity of 1.1m/s.

C. Variable Touchdown Stiffness Experiments

To simulate the lander's touchdown process under various stiffness conditions, a series of experiments are conducted. The results are depicted in Fig 17(6.4N/mm), Fig. 18(11.2N/mm), and Fig 19(16.0N/mm). The compensation force is consistently set at 2813N, while the velocity ranges from 0.4 to 1.1m/s.

Experiments with varying contact stiffness demonstrate that lower stiffness results in a slower rate of force change during touchdown. Specifically, at a contact stiffness of 6.4 N/mm, the force error during touchdown is smaller than in the other groups. Notably, there is a positive deviation in the control force at velocities of 0.4 m/s and 0.6 m/s. Similarly, the force error at 0.8 m/s and 1.1 m/s is also reduced, remaining within 40 N at a contact stiffness of 6.4 N/mm.

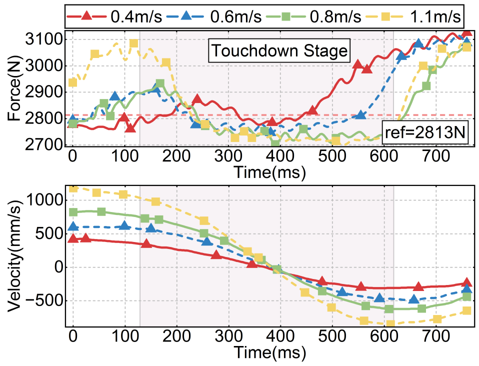

Fig. 18. Touchdown experiment with 11.2N/mm contact stiffness. Results of velocity 0.4m/s-1.1m/s are shown.

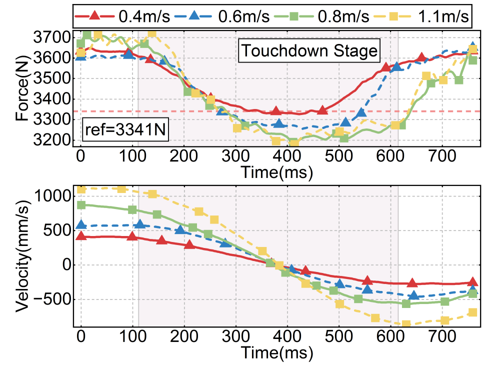

Fig. 20. Touchdown experiment with 3341N target force. Results of velocity 0.4m/s-1.1m/s are shown.

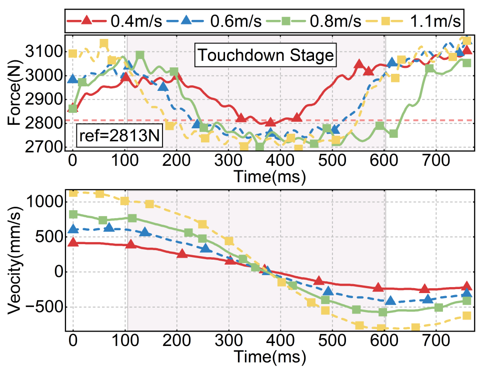

Fig. 19. Touchdown experiment with 16.0N/mm contact stiffness. Results of velocity 0.4m/s-1.1m/s are shown.

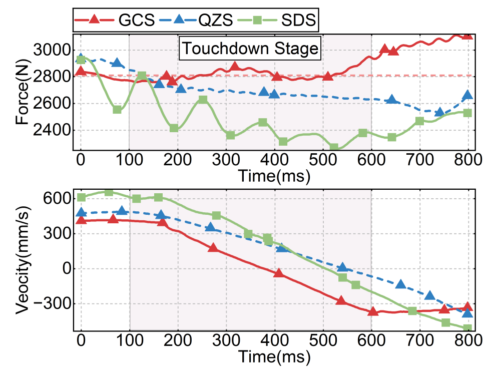

Fig. 21. Touchdown experiment of GCS compared with QZS and SDS in 0.4m/s velocity.

In a hypothetical scenario with 0 N/mm contact stiffness, which is equivalent to the lander undergoing free fall, the system is designed to maintain its previous motion state, keeping the lever stationary. This trend in the ideal experiment closely aligns with the actual experimental results.

Comparing the 11.2 N/mm and 16 N/mm stiffness experiments, it's clear that the 16 N/mm case has a shorter touchdown duration. Unlike the 6.4 N/mm results, this experiment shows a longer touchdown duration. Analyzing the 3 groups with different ground contact stiffness levels, higher impact velocities are seen to extend touchdown durations. Across 3 stiffness conditions, the controller consistently maintains stable force deviation and high accuracy.

D. Variable Target Force Experiments

By increasing the lander's mass to 409kg, the target compensation force is set at 3341N, and the QZS's output force is fine-tuned by adjusting the springs. With a contact stiffness of 11.2N/mm, a series of touchdown experiments are conducted at various velocities under the increased compensation force, as illustrated in Fig. 20. The experiments with a target force of 2813N(Fig. 18) and those with 3341N as the target force exhibit similar outcomes. In the 2813N experiments, the peak force error is 53.67N(1.9%) at a velocity of 0.4m/s, increasing to 111.99N(4.0%) at 1.1m/s. Similarly, the 3341N experiments demonstrate a maximum force error of 14.02N(0.4%) at 0.4 m/s and 162.15N(4.8%) at 1.1m/s. Furthermore, the duration of the touchdown process remains nearly identical in both experiments. Consequently, it can be inferred that the proposed controller is robust against variations in the lander's mass.

E. Comparison Experiments With QZS and SDS

To assess the proposed GCS's effectiveness, comparative experiments are conducted at a touchdown velocity of 0.4m/s, with a target force of 2813N and a contact stiffness of 11.2N/mm. The GCS's control efficacy is compared against the QZS and SDS force compensation results(Fig. 21), highlighting the GCS's superior control performance.

The SDS exhibits significant fluctuations in force error during the touchdown process, with a peak force error of 550N, accompanied by pronounced oscillations. In contrast, the QZS maintains a relatively stable force throughout the touchdown process, with a compensation force error that is relatively smaller compared to the SDS(approximately 250N), albeit without a converging trend. Due to the absence of active force regulation, the compensation force error increases further as the touchdown phase progresses. Furthermore, the GCS demonstrates a stable force deviation of approximately 40N, with a maximum error of 1.4%.

The suboptimal control performance of the SDS is predictable. The high stiffness of the cable means that minor position fluctuations, caused by the servomotor's speed control commands, lead to substantial force deviations at the endpoint. This contributes to oscillations during motion. Additionally, the unpredictable nature of the touchdown environment impedes the controller's ability to determine the exact moment of touchdown, preventing the enhancement of system response speed through feed-forward compensation. Limited by the control system's bandwidth and exacerbated by the cable's high stiffness, the SDS demonstrates a narrow phase margin and an inadequate response speed to force deviations during touchdown. This results in significant force deviations.

Theoretically, the QZS should maintain a consistent force in a quasi-static environment. However, practical challenges, including friction and inaccuracies in spring stiffness, prevent the QZS from realizing an ideal quasi-zero stiffness state. The relationship between the QZS's output force curve and the lever angle is illustrated in Fig. 1. Within the specified operational range, the QZS exhibits 2 primary issues:

1) hysteresis phenomenon in the force curve.
2) force-angle stiffness is 8.3N/deg instead of 0N/deg.

The hysteresis observed in the force curve signifies that the output force is influenced by the direction of the lever's movement, typically attributable to friction within the mechanism. When comparing the hysteresis force value of the stiffness curve with the touchdown force curve from the QZS experiment, it is evident that both exhibit a force error of approximately 250N. This correlation suggests that the accuracy of force compensation in the QZS is compromised by frictional effects.

The non-zero force-angle stiffness is mainly due to the inherent errors in the QZS mechanism. In practical experiments, errors in spring stiffness lead to deviations in the pre-tensioning length, introducing non-zero stiffness and tension deviations in the QZS. While this does compromise the accuracy of the QZS, it is important to note that it also broadens the system's operational range. Ideally, a spring with specific stiffness should be custom-designed for each pulling force magnitude. However, by adjusting the pre-tensioning length, a set of springs with specific stiffness, supported by the SDS controller, can adapt to a wide range of target force variations with minimal compensation accuracy loss(theoretical analysis is detailed in remark 1, where it is explained that the force deviation f_{dk} due to QZS spring stiffness error may not lead to the loss of QZS passivity). Our experiments showed that a set of springs with specific stiffness could handle a force range of approximately $\pm$50N.

V. Conclusion

This paper proposed a large-scale and high accuracy GCS to provide a low-gravity environment for the lander touchdown experiment. To address the limitations of traditional quasi-zero stiffness(QZS) methods in terms of accuracy and operational range, a servo-driven system is proposed and integrated with QZS to form a composite system. The input-output dynamic characteristics of the gravity compensation system(GCS) are analyzed using passivity theory, providing a theoretical explanation for the compensation errors in QZS. The conditions for the global asymptotic stability of GCS are derived, and a fuzzy controller is introduced to regulate the system's equilibrium point and convergence speed, ensuring rapid error reduction in force compensation. With the proposed control law, the maximum force compensation error is reduced from 13.9% to 4.0%, while the supported simulation range expands from 800 mm to over 12,000 mm. Additionally, the robustness of the controller against external disturbances is demonstrated, and parameter design guidelines for practical applications of GCS are provided. Various physical experiments are conducted on the experimental platform, verifying the effectiveness of the proposed system. Compared to other low-gravity simulation methods in Table I, this study achieves satisfactory performance in terms of supported motion range, motion velocity, and force compensation accuracy.

References

[1] A. Witze, "Moon mission failure: Why is it so hard to pull off a lunar landing?" *Nature*. Accessed: Jan. 9, 2024. [Online]. Available: https://www.nature.com/articles/d41586-023-01454-7

[2] H. Yin et al., "Review on soft landing buffer systems for planetary exploration," *Acta Astronautica*, vol. 228, pp. 561–594, Mar. 2025.

[3] W. Jackie, "Head of Russian space agency offers context on why spacecraft crashed into the moon," CNN. [Online]. Available: https://edition.cnn.com/2023/08/21/world/russia-luna-25-crash-cause-engine-issue-scn/index.html

[4] J. O'Callaghan, "Russian moon lander crash—What happened, and what's next?," *Nature*. Accessed: Jan. 9, 2024. [Online]. Available: https://www.nature.com/articles/d41586-023-02659-6

[5] W. Mike, "Private Odysseus moon lander broke a leg during historic touchdown," Space. Accessed: Feb. 21, 2025. [Online]. Available: https://www.space.com/intuitive-machines-odysseus-moon-lander-broken-leg

[6] D. Ren et al., "Ground-test validation technologies for chang'e-5 lunar probe," *Scientia Sinica Technologica*, vol. 51, no. 7, pp. 778–787, Jul. 2021.

[7] C. Menon et al., "Issues and solutions for testing free-flying robots," *Acta Astronautica*, vol. 60, no. 12, pp. 957–965, Jun. 2007.

[8] T. Rybus and K. Seweryn, "Planar air-bearing microgravity simulators: Review of applications, existing solutions and design parameters," *Acta Astronautica*, vol. 120, pp. 239–259, Mar. 2016.

[9] C. R. Carignan and D. L. Akin, "The reaction stabilization of on-orbit robots," *IEEE Control Syst. Mag.*, vol. 20, no. 6, pp. 19–33, Dec. 2000.

[10] H. Sanavandi and W. Guo, "A magnetic levitation based low-gravity simulator with an unprecedented large functional volume," *NPJ Microgr.*, vol. 7, no. 1, pp. 1–7, Oct. 2021.

[11] Y. Wei, X. Yang, Z. Xu, and X. Bai, "Novel ground microgravity experiment system for a spacecraft-manipulator system based on suspension and air-bearing," *Aerosp. Sci. Technol.*, vol. 141, Oct. 2023, Art. no. 108587.

[12] J. Molina, G. Bisiacchi, L. Reyes, E. Vicente, F. Contreras, and M. Mesinas, "Three-axis-air bearing based platform for small satellite attitude determination and control simulation," *J. Appl. Res. Technol.*, vol. 3, no. 3, pp. 222–237, Dec. 2005.

[13] R. Zappulla, J. Virgili-Llop, C. Zagaris, H. Park, and M. Romano, "Dynamic air-bearing hardware-in-the-loop testbed to experimentally evaluate autonomous spacecraft proximity maneuvers," *J. Spacecraft Rockets*, vol. 54, no. 4, pp. 825–839, Jul. 2017.

[14] M. I. Al-Majed and B. N. Alsuwaidan, "A new testing platform for attitude determination and control subsystems: Design and applications," in *Proc. IEEE/ASME Int. Conf. Adv. Intell. Mechatronics*, Jul. 2009, pp. 1318–1323.

[15] W. Yuemin, L. Qiang, W. Xian, L. Ying, and S. Jianhui, "Design and verification of air-floating suspension gravity compensation device for solar wing," *J. Mech. Eng.*, vol. 56, no. 13, p. 149, 2020.

[16] Z. Deng, Z. Liu, H. Gao, and L. Ding, "An approach for gravity compensation of planetary rovers," in *Proc. 3rd Int. Symp. Syst. Control Aeronaut. Astronaut.*, Jun. 2010, pp. 1053–1058.

[17] K. Saulnier, D. Pérez, R. C. Huang, D. Gallardo, G. Tilton, and R. Bevilacqua, "A six-degree-of-freedom hardware-in-the-loop simulator for small spacecraft," *Acta Astronautica*, vol. 105, no. 2, pp. 444–462, Dec. 2014.

[18] G. C. White and Y. Xu, "An active vertical-direction gravity compensation system," *IEEE Trans. Instrum. Meas.*, vol. 43, no. 6, pp. 786–792, Dec. 1994.

[19] F. Elhardt et al., "The motion suspension system for on-ground tests of space robots: Demonstration and results," in *Proc. IEEE Aerosp. Conf.*, Mar. 2024, pp. 1–9.

[20] N. Paine, S. Oh, and L. Sentis, "Design and control considerations for high-performance series elastic actuators," *IEEE/ASME Trans. Mechatronics*, vol. 19, no. 3, pp. 1080–1091, Jun. 2014.

[21] K.-Y. Lin, K.-Y. Wu, and C.-C. Lan, "High-performance series elastic stepper motors for interaction force control," in *Proc. IEEE Int. Conf. Adv. Intell. Mechatronics (AIM)*, Jul. 2017, pp. 773–778.

[22] P. Wang and Q. Xu, "Design and modeling of constant-force mechanisms: A survey," *Mechanism Mach. Theory*, vol. 119, pp. 1–21, Jan. 2018.

[23] Z.-W. Yang and C.-C. Lan, "An adjustable gravity-balancing mechanism using planar extension and compression springs," *Mechanism Mach. Theory*, vol. 92, pp. 314–329, Oct. 2015.

[24] J. Jia, Y. Jia, and S. Sun, "Preliminary design and development of an active suspension gravity compensation system for ground verification," *Mechanism Mach. Theory*, vol. 128, pp. 492–507, Oct. 2018.

[25] M. Duan, J. Jia, and T. Ito, "Fast terminal sliding mode control based on speed and disturbance estimation for an active suspension gravity compensation system," *Mechanism Mach. Theory*, vol. 155, Jan. 2021, Art. no. 104073.

[26] M. Yang, Z. Xu, Y. He, Y. Liu, and B. Wang, "Zero gravity tracking system using constant tension suspension for a multidimensional framed structure space antenna," in *Proc. 7th Int. Conf. Mech. Aerosp. Eng. (ICMAE)*, Jul. 2016, pp. 614–621.

[27] J. Qu, *The control research of suspended low gravity simulation system*, Master thesis, Harbin Institute of Technology, Harbin, China, 2018.

[28] M. Frey, G. Colombo, M. Vaglio, R. Bucher, M. Jorg, and R. Riener, "A novel mechatronic body weight support system," *IEEE Trans. Neural Syst. Rehabil. Eng.*, vol. 14, no. 3, pp. 311–321, Sep. 2006.

[29] A. Nakayama, T. Hirata, and K. Tsujita, "A study of a gravity compensation system for the spacecraft prototype test by using multi-robot system," *Artif. Life Robot.*, vol. 25, no. 1, pp. 81–88, Feb. 2020.

[30] D. A. Kienholz, E. F. Crawley, and T. J. Harvey, "Very low frequency suspension systems for dynamic testing," in *Proc. 30th Struct., Struct. Dyn. Mater.*, Apr. 1989, pp. 327–336. Accessed: Sep. 5, 2023.

[31] R. Zhou et al., "Gravity compensation method via magnetic quasi-zero stiffness combined with a quasi-zero deformation control strategy," *Sci. China Technol. Sci.*, vol. 65, no. 8, pp. 1738–1748, Aug. 2022.

[32] Z. Zhao, K. Fu, M. Li, J. Li, and Y. Xiao, "Gravity compensation system of mesh antennas for in-orbit prediction of deployment dynamics," *Acta Astronautica*, vol. 167, pp. 1–13, Feb. 2020.

[33] D. Xiong, Y. Huang, Y. Yang, H. Liu, Z. Jiang, and W. Han, "Research on horizontal following control of a suspended robot for self-momentum targets," in *Proc. IEEE Int. Conf. Robot. Biomimetics (ROBIO)*, Dec. 2023, pp. 1–6.

[34] F. Niu, Z. Liu, H. Gao, H. Yu, N. Li, and Z. Deng, "An enhanced cascade constant-force system based on an improved low-stiffness mechanism," *Mechanism Mach. Theory*, vol. 167, Jan. 2022, Art. no. 104544.

[35] Z. Liu et al., "Design, analysis, and experimental validation of an active constant-force system based on a low-stiffness mechanism," *Mechanism Mach. Theory*, vol. 130, pp. 1–26, Dec. 2018.

[36] H. Sun, X. Tang, and S. S. Ge, "Advancing Mars exploration: Development of a large-scale gravity compensation system for landers during descent," *IEEE Trans. Aerosp. Electron. Syst.*, vol. 61, no. 3, pp. 1–14, Jun. 2025.

[37] B. Ding, J. Zhao, and Y. Li, "Design of a spatial constant-force end-effector for polishing/deburring operations," *Int. J. Adv. Manuf. Technol.*, vol. 116, nos. 11–12, pp. 3507–3515, Oct. 2021.

[38] B. Ding, X. Li, S.-C. Chen, and Y. Li, "Modular quasi-zero-stiffness isolator based on compliant constant-force mechanisms for low-frequency vibration isolation," *J. Vibrat. Control*, vol. 30, nos. 13–14, pp. 3006–3020, Jul. 2024.

[39] Y. Wu, N. Sun, H. Chen, and Y. Fang, "Adaptive output feedback control for 5-DOF varying-cable-length tower cranes with cargo mass estimation," *IEEE Trans. Ind. Informat.*, vol. 17, no. 4, pp. 2453–2464, Apr. 2021.

[40] R. J. Caverly and J. R. Forbes, "Dynamic modeling and noncollocated control of a flexible planar cable-driven manipulator," *IEEE Trans. Robot.*, vol. 30, no. 6, pp. 1386–1397, Dec. 2014.

[41] R. J. Caverly, J. R. Forbes, and D. Mohammadshahi, "Dynamic modeling and passivity-based control of a single degree of freedom cable-actuated system," *IEEE Trans. Control Syst. Technol.*, vol. 23, no. 3, pp. 898–909, May 2015.

[42] A. Van Der Schaft, *L2-Gain and Passivity Techniques in Nonlinear Control* (Communications and Control Engineering). Cham, Switzerland: Springer, 2017.

[43] M. Arcak, C. Meissen, and A. Packard, *Networks of Dissipative Systems: Compositional Certification of Stability, Performance, and Safety*, 1st ed., Cham, Switzerland: Springer, Mar. 2016.

[44] U. J. Blanchard, Evaluation of a Full-Scale Lunar-Gravity Simulator by Comparision of Landing-Impact Tests of a Full-scale and a 1/6-Scale Model, Standard NASA TN D-4474, 1968.

[45] U. J. Blanchard, Full-Scale Dynamic Landing-Impact Investigation of a Prototype Lunar Module Landing Gear, Standard NASA TN D-5029, 1969.

[46] G. A. Zupp, An Analysis and a Historical Review of the Apollo Program Lunar Module Touchdown Dynamics, Standard NASA SP-2013-605, 2013.

[47] J. Zhai, "Energy absorption characteristics and soft landing performance of origami honeycomb buffer device," Ph.D. dissertation, Dept. Mech. Eng., Nanjing Univ. Sci. Technol., Nanjing, China, 2023.

[48] H. Sun, "Design of lunar soft landing cushion foot and simulation study on landing cushioning performance," Master's thesis, Dept. Mech. Eng., Harbin Univ. Sci. Technol., Harbin, China, 2024.

[49] J. G. De Jalón and E. Bayo, *Kinematic and Dynamic Simulation of Multibody Systems: The Real-Time Challenge* (Mechanical Engineering Series). NY, NY, USA: Springer, 1994.

[50] A.-T. Nguyen, T. Taniguchi, L. Eciolaza, V. Campos, R. Palhares, and M. Sugeno, "Fuzzy control systems: Past, present and future," *IEEE Comput. Intell. Mag.*, vol. 14, no. 1, pp. 56–68, Feb. 2019.

[51] G. Feng, "A survey on analysis and design of model-based fuzzy control systems," *IEEE Trans. Fuzzy Syst.*, vol. 14, no. 5, pp. 676–697, Oct. 2006.

[52] C. C. Lee, "Fuzzy logic in control systems: Fuzzy logic controller. I," *IEEE Trans. Syst., Man, Cybern.*, vol. 20, no. 2, pp. 404–418, Mar. 1990.

[53] H. Sun, X. Tang, X. Wang, and Q. Cong, "Research on the tracing accurate of force based on fuzzy-pi control for a high-speed landing system," *J. Brazilian Soc. Mech. Sci. Eng.*, vol. 43, no. 4, pp. 217–227, Mar. 2021.

Rongqiao Zhang received the B.S. degree in mechanical engineering from Tsinghua University, Beijing, China, in 2021, where he is currently pursuing the Ph.D. degree in mechanical engineering. His research interests include the modeling, identification, and force control of cable-driven parallel robots.

Zhengqing Li received the B.S. degree in mechanical engineering from Tsinghua University, Beijing, China, in 2022, where he is currently pursuing the Ph.D. degree in mechanical engineering. His research interests include cable-driven parallel robots, force control, and lower limb exoskeletons.

Haining Sun (Member, IEEE) received the B.Eng. degree in mechanical engineering from Shandong University, Jinan, China, in 2017, and the Ph.D. degree in mechanical engineering from Tsinghua University, Beijing, China, in 2022. He is currently with Singapore Institute of Manufacturing Technology, Singapore. His current research interests include cable-driven robots, vibration control, dynamic control, and force control.

Xiaoqaing Tang received the Ph.D. degree in mechanical engineering from Tsinghua University, Beijing, China, in 2001. He is currently a Professor with the Department of Mechanical Engineering, Tsinghua University. His research interests include parallel manipulators, robots, and reconfigurable manufacturing technology.